Volume 19
Number 14
14 April 2023
Pages 2457–2666

Soft Matter

rsc.li/soft-matter-journal

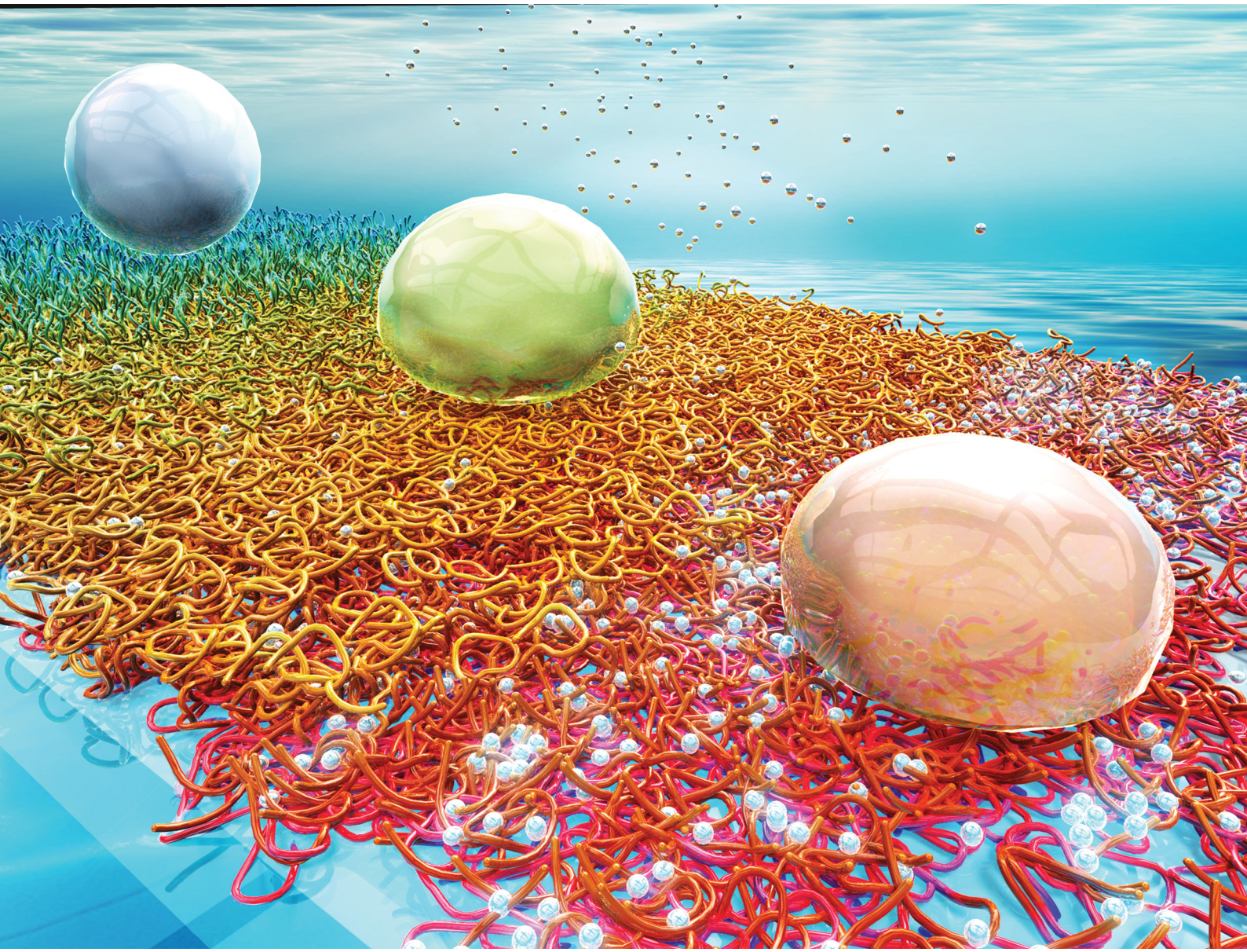

ISSN 1744-6848

ROYAL SOCIETY OF CHEMISTRY

PAPER

Marcus Müller, Motomu Tanaka *et al.*
Modulation of wetting of stimulus responsive polymer brushes by lipid vesicles: experiments and simulations

Soft Matter

PAPER

View Article Online
View Journal | View Issue

Cite this: *Soft Matter*, 2023, **19**, 2491

Modulation of wetting of stimulus responsive polymer brushes by lipid vesicles: experiments and simulations†

Felix Weissenfeld,‡[a] Lucia Wesenberg,‡[b] Masaki Nakahata,[cd] Marcus Müller *[b] and Motomu Tanaka *[ae]

Received 20th December 2022,
Accepted 10th February 2023

DOI: 10.1039/d2sm01673g

rsc.li/soft-matter-journal

The interactions between vesicle and substrate have been studied by simulation and experiment. We grafted polyacrylic acid brushes containing cysteine side chains at a defined area density on planar lipid membranes. Specular X-ray reflectivity data indicated that the addition of Cd^{2+} ions induces the compaction of the polymer brush layer and modulates the adhesion of lipid vesicles. Using micro-interferometry imaging, we determined the onset level, [$CdCl_2$] = 0.25 mM, at which the wetting of the vesicle emerges. The characteristics of the interactions between vesicle and brush were quantitatively evaluated by the shape of the vesicle near the substrate and height fluctuations of the membrane in contact with brushes. To analyze these experiments, we have systematically studied the shape and adhesion of axially symmetric vesicles for finite-range membrane–substrate interaction, *i.e.*, a relevant experimental characteristic, through simulations. The wetting of vesicles sensitively depends on the interaction range and the approximate estimates of the capillary length change significantly, depending on the adhesion strength. We found, however, that the local transversality condition that relates the maximal curvature at the edge of the adhesion zone to the adhesion strength remains rather accurate even for a finite interaction range as long as the vesicle is large compared to the interaction range.

1 Introduction

Physical contact of cells to their neighbors – cell adhesion – plays a key role in a wide variety of biological processes. Cell adhesion modulates a number of biochemical signaling pathways[1,2] and tissue morphogenesis driven by forces acting between neighboring cells.[3] On the other hand, impaired cell adhesion function is often associated with diseases, such as cancer metastasis. A significant reduction of cell–cell and cell–matrix adhesion causes the invasive migration and release of cancer cells into blood circulation.[4] Ample evidence has indicated that cell adhesion is not only a static attachment between cells but also highly dynamic. For example, the freshwater polyp Hydra is able to regenerate the complete body with a new head and foot by *de novo* pattern formation from dissociated single cells by sorting cell–cell contacts.[5,6] On the molecular level, an increasing number of experimental studies have shown that the dynamic rearrangement of adhesion molecules and their ligands plays critical roles in immunological response[7] and cell apoptosis.[8] Such experimental findings have been qualitatively recapitulated by using a phenomenological model of adhesion-induced phase separation[9] or by assuming the presence of strong pinning centers.[10] However, the quantitative combination of experiments and simulations still remains challenging.

Therefore, a large number of studies so far have been performed to physically model cell adhesion using rather simple, artificial lipid vesicles in the presence and absence of specific ligand–receptor-like interaction pairs (stickers). Cell adhesion in equilibrium has been described within the framework of wetting physics, irrespective of the different origins of adhesion on the molecular level.[11–14] In analogy to the shape of liquid drops on substrates, the shape of a cell or a lipid vesicle can be fine-tuned by tailoring the membrane–substrate interaction, $V(z)$, that quantifies the free energy of placing a unit area of the membrane a distance, z, away from the substrate. $V(z)$ is

[a] *Physical Chemistry of Biosystems, Institute of Physical Chemistry, Heidelberg University, 69120 Heidelberg, Germany. E-mail: tanaka@uni-heidelberg.de*
[b] *Institute for Theoretical Physics, Georg-August University, Friedrich-Hund-Platz 1, 37077 Göttingen, Germany. E-mail: mmueller@theorie.physik.uni-goettingen.de*
[c] *Department of Materials Engineering Science, Graduate School of Engineering Science, Osaka University, 560-8531 Osaka, Japan*
[d] *Department of Macromolecular Science, Graduate School of Science, Osaka University, 560-8531 Osaka, Japan*
[e] *Center for Advanced Study, Institute for Advanced Study, Kyoto University, 606-8501 Kyoto, Japan*

† Electronic supplementary information (ESI) available. See DOI: https://doi.org/10.1039/d2sm01673g

‡ These authors contributed equally.

characterized by the interplay of short- and long-range forces. Notably, what makes "biological" droplets, such as cells and lipid vesicles, distinct from droplets of simple liquid is the interface between the interior and exterior; the bilayer lipid membrane. The intrinsic physical property of lipid bilayer membranes is their bending rigidity, κ, whereas the bilayer tension, γ, depends on the membrane geometry. Conversely, the tension of the liquid–vapor interface of a liquid drop is an intrinsic property, independent of the drop shape.[15–17] Another difference is that the shape of an adhered vesicle is dictated by the balance between adhesion and bending free energies, whereas the shape of a liquid drop is determined by balancing adhesion and interface tension. The latter balance – resulting in Young's equation[18] for the contact angle of a drop – remains invariant under scale changes of the liquid drop, whereas the former balance explicitly depends on the vesicle size, R_0. Thus, one can systematically study the adhesion of vesicles by varying the vesicle size, leaving the substrate chemistry unaltered.

From the experimental viewpoint, the use of soft polymer substrates is a straightforward strategy to finely adjust the adhesion of vesicles by tuning vesicle–substrate interaction, $V(z)$. Planar lipid membranes deposited on polymer substrates – called polymer-supported membranes[19] – have been used as soft "cushions" that reduce the frictional coupling of membranes and membrane-associated proteins by preventing direct contact.[20,21] Previously, we measured specular neutron and X-ray reflectivity of zwitterionic phosphatidylcholine membranes deposited on about 20 and 40 nm-thick cellulose supports.[22] The equilibrium distance between the membrane and underlying Si substrates determined by experiments could be reproduced by calculating the disjoining pressure including van der Waals, hydration, and Helfrich-undulation repulsion, quantitatively.

To switch the adhesion of vesicles, the use of stimulus responsive polymer brushes is a promising strategy, as they can change their physical properties (conformation, degrees of ionization, solvent affinity, *etc.*) by external cues, such as changes in temperature, pH, light, and ions.[23–31] Previously, we transferred pH-responsive diblock copolymers from the air/water interface to solid substrates and demonstrated the change in polymer-chain conformation by pH titration. Intriguingly, the reversible change in polymer chain conformation led to a switching of the water layer between the membrane and brushes.[32]

In this study, we designed switchable polymer-brush substrates that can switch $V(z)$ by forming chelator complexes with divalent ions in a concentration-dependent manner. We synthesized polyacrylic acid brushes containing cysteine side chains terminated with biotin (PAA-Cys5-biotin) based on the hypothesis that –COOH and –SH side chains form a complex with Cd^{2+} ions with a high affinity.[33] To achieve a uniform grafting of brushes at a defined grafting density, we grafted the polymer chains onto supported membranes doped with biotin-functionalized lipids *via* neutravidin crosslinkers, instead of the commonly used "grafting onto" strategy.[34,35] Owing to the extremely high affinity of biotin and neutravidin, $K_D \approx 10^{-15}$ M,[36] the average grafting distance, $\langle d \rangle$ can be controlled at nm accuracy simply by the doping ratio of biotin lipids (see Methods for more details). In contrast to previous studies, which induced the change in areal charge density by a drastic change in solution pH[37] or salt concentrations,[38] PAA-Cys5 brushes enable us to switch the conformation and hence $V(z)$ in the presence of 100 mM NaCl with 10 mM Tris buffer (pH 7.4), where the change in the total ionic strength and pH is negligible. The change in thickness, roughness, and density of the polymer brush layer was monitored by specular X-ray reflectivity, while the curvature of the effective membrane–substrate interaction was calculated from the height fluctuation of the membranes in contact with brushes. The global shape of vesicles (side view) was reconstructed from the confocal fluorescence microscopy images and compared to the theory.

In the simulation, we represent the membrane by a thin elastic sheet within the Helfrich model[15] that has previously been utilized to study the adsorption of vesicles.[12,13,39–41] We are describing the shape through a Fourier expansion around a spherical vesicle.[42,43] Numerically minimizing the bending and adhesion, we determine the optimal shape of the vesicle paying particular attention to the effect of a finite range of the interaction, V, between membrane and substrate. This effect is present in the experiment and has to be accounted for in the quantitative analysis.

Our manuscript is arranged as follows: in the next section, we introduce the experimental system and methods, followed by a description of the simulation model and numerical techniques. In the result section, we study the thermodynamics of adhesion and vesicle shape and present results on the experimental switching of the brush and the curvature of the vesicle–brush interaction. The manuscript closes with a brief summary and outlook.

2 Materials, models, and methods

2.1 Experimental materials

2.1.1 Chemicals. Milli-Q water from an ultra purification system (Merck Millipore, Darmstadt, Germany) with a resistance >18 MΩ cm was used for all experiments. All the 1,2-dioleoyl-*sn-glycero*-3-phosphocholine (DOPC), 1,2-dioleoyl-*sn-glycero*-3-phosphoethanolamine-*N*-(cap biotinyl) (DOPE-biotin), Texas Red™ 1,2-dihexadecanoyl-*sn*-glycerin-3-phosphoethanolamine (DHPE-Texas Red) were purchased from Avanti Polar Lipids (Alabama, USA). Neutravidin was purchased from Thermo Fisher Scientific (Karlsruhe, Germany) and was ultracentrifuged before use (100.000 *g*, 1 h). The supernatant was used for the experiments. Unless stated otherwise, the other chemicals were purchased from Sigma-Aldrich (Taufkirchen, Germany).

2.1.2 Synthesis of PAA-Cys5-biotin. PAA-Cys5-biotin (Fig. 1) was synthesized through copolymerization of *S*-trityl-cysteine acrylamide (*S*-Tri-Cys-AAm) and acrylic acid (AA) using 4,4′-((*E*)-diazene-1,2-diyl)bis(4-cyano-*N*-(2-(5-((3*aR*,4*R*,6*aS*)-2-oxohexahydro-1*H*-thieno[3,4-*d*]imidazol-4-yl)pentanamido)ethyl)pentanamide) (ACVA-biotin) as an initiator and 2-(dodecylthiocarbonothioylthio)-2-methylpropionic acid (DDMAT) as a chain transfer agent, followed by deprotection of trityl group with trifluoroacetic acid (TFA). In brief: *S*-Tri-Cys-AAm (0.05 mmol), AA (0.95 mmol), ACVA-biotin (0.01 mmol), and DDMAT (0.01 mmol) were dissolved in 1 mL of dimethylsulfoxide (DMSO) dried with

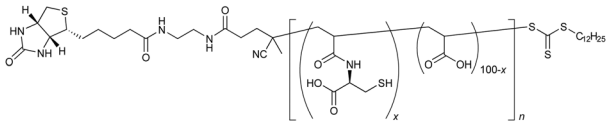

Fig. 1 Chemical structure of stimulus responsive PAA-Cys5-biotin possessing both –COOH and –SH groups.

molecular sieves 4A. The solution was purged with nitrogen gas for 1 h, sealed, and heated in an oil bath at 70 °C overnight. The solution was poured into acetone (10 mL) with stirring. The resultant oily precipitate was collected with centrifugation (3500 rpm, 5 min). After removing the supernatant by decantation, trifluoroacetic acid (TFA) (1 mL) was added and stirred overnight. The solution was poured into diethyl ether (10 mL). The resultant solid precipitate was washed with diethyl ether (10 mL) three times and dried in a vacuum at room temperature. Successful polymerization and deprotection were confirmed by ^{1}H NMR spectra recorded at 400 MHz with a JNM-ECS400 NMR spectrometer (JEOL, Tokyo, Japan). Gel permeation chromatography (GPC) analysis of PAA-Cys5-biotin was carried out using a GL-7400 HPLC system (GL Science, Tokyo, Japan) equipped with Inertsil WP300 Diol column (GL Science, Tokyo, Japan) and refractive index (RI) detector (RID-20A, Shimadzu, Kyoto, Japan), using PBS as an eluent at the flow rate of 0.3 mL min^{-1}. at 25 °C. ReadyCal-Kit Pullulan (purchased from PSS Polymer Standards Service GmbH, Mainz, Germany) was used as the calibration standard. The weight average molecular weight (M_w) and polydispersity index (M_w/M_n) of PAA-Cys5-biotin were estimated to be $M_w = 7.4 \times 10^4$ Da and $M_w/M_n = 2.5$, respectively.

2.2 Methods

2.2.1 Fabrication of switchable substrates. Lipid stock solutions in chloroform (1 mg mL^{-1}) containing 98 mol% DOPC and 2 mol% DOPE-biotin were stored in a vacuum oven overnight. The dried lipid mixture was suspended in a Tris (10 mM) buffer containing 100 mM NaCl (pH 7.4). Small unilamellar vesicles (SUVs) were prepared by sonication of a lipid suspension with a Misonix Sonicator 3000 (Misonix, Düsseldorf, Germany). A supported membrane was deposited on a cleaned glass slide by incubating vesicle suspension[44,45] for 30 min at 40 °C, and the unbound SUVs were carefully removed by rinsing. In the next step, the sample was incubated with neutravidin (40 μg mL^{-1}) for 1 h at 40 °C. After removing unbound neutravidin, the solution of PAA-Cys5-biotin (40 μg mL^{-1}) was injected and incubated under the same conditions.

2.2.2 Preparation of giant unilamellar vesicles. Giant unilamellar vesicles (GUVs) were prepared by electroswelling as reported previously.[46] In brief: indium tin oxide (ITO) coated glass slides (Sigma-Aldrich) were spin-coated with DOPC including 0.2 mol% DHPE-Texas Red. The dried lipid mixture was hydrated with sucrose solution under AC potentials (10 Hz, 3 V) at 37 °C for 2 h. A 0.2 mL portion of the vesicle suspension was mixed with 1 mL of solutions with controlled density and osmolality for each experiment. For example, to enable the adhesion of vesicles to the substrates coated with PAA-Cys5 brushes, the vesicles were suspended in 340 mM glucose solution buffered with 10 mM Tris to achieve the density difference of $\Delta\rho \approx 40$ kg m^{-3}. For the experiments in the absence of Tris buffer (*cf.* Section 3.1), the vesicles were suspended in 360 mM glucose solution ($\Delta\rho \approx 38$ kg m^{-3}). The osmolality was measured and adjusted using a micro-osmometer (OM 806, Löser, Berlin, Germany).

2.2.3 Confocal fluorescence microscopy imaging of global vesicle shape. The global shape of GUVs was captured with a Nikon A1R confocal microscope (Nikon Europe, Düsseldorf, Germany) 60× oil immersion objective (NA 1.40). For the fluorescence imaging, GUVs were labeled by incorporating 0.2 mol% of DHPE-Texas Red. The vesicles were deposited on brush substrates pre-equilibrated with [$CdCl_2$] = 0–1.0 mM for 30 min before the imaging. Confocal side view images were obtained due to confocal 3D reconstruction of confocal bottom view images with a stepsize of 0.5 μm using ImageJ. The distortion of the reconstructed image in the *z*-direction was corrected using the images of commercially available fluorescently labeled latex particles with a similar size (R = 7.5 μm).

2.2.4 Specular X-ray reflectivity. X-ray reflectivity curves were measured using a D8 Advance diffractometer (Bruker, Germany) operating with a sealed X-ray tube emitting Mo K_α radiation (E = 17.48 keV, λ = 0.0709 nm). The beam size was defined as 200 μm in the scattering plane after its collimation by various slits. To avoid the sample radiation damage, the attenuator was set to automatic. The cleaned Si wafers were placed into a Teflon chamber with Kapton windows, and the momentum transfer normal to the plane of the membrane is given as a function of the angle of incidence α_i,

$$q_z = \frac{4\pi}{\lambda}\sin\alpha_i \qquad (1)$$

The reflectivity for each data point was corrected for the beam footprint and for the beam intensity. A generic minimization algorithm of the Parratt formalism[47] implemented in the Motofit software[48] was used to fit the experimental data.

2.2.5 Label-free, microinterferometry imaging of vesicle/brush contact. The interaction between vesicles and brush substrates was monitored by label-free, reflection interference contrast microscopy (RICM).[10,49,50] RICM imaging was performed on an Axio Observer Z1 microscope (Zeiss, Oberkochen, Germany) equipped with a 63× oil immersion objective (NA 1.25) with a built-in $\lambda/4$ plate. To record multiple interferences, the Illumination Numerical Aperture (INA) was adjusted to 0.48, and about 400 consecutive images were collected by an Orca-Flash4.0LT camera (Hamamatsu Photonics, Herrsching, Germany) at an exposure time of 30 ms, and were subjected to the analysis. The intensity I was converted to the relative height δz *via*:

$$I(\delta z) = I_1 + I_2 + 2\sqrt{I_1 I_2}\cos(2k\delta z(x,y) + \Phi) \qquad (2)$$

I_i represents the intensity of the light reflected at the ith interface, and $k = \frac{2\pi n}{\lambda}$ is the wave vector. n is the refractive index of the buffer (n = 1.344), λ the wavelength (λ = 475 nm), and Φ the phase shift of the reflected light. To monitor the height fluctuation $\delta z(t)$, we collected the mean intensity from

3×3 pixels as a function of time $I(t)$:

$$\delta z(t) = \arccos\left(\frac{2I(t) - (I_{\max} + I_{\min})}{(I_{\max} - I_{\min})}\right)\frac{\lambda}{4\pi n} \tag{3}$$

$I_{\max}$ and $I_{\min}$ are the intensity minima and maxima of the background. The analyses were performed using a self-written Matlab routine (R2019a).[10]

2.3 Model and numerical techniques

2.3.1 Description of vesicle shape. We limit our considerations to axially symmetric vesicles using cylindrical coordinates, (z,r). The membrane area $A_0 = 4\pi {R_0}^2$ is fixed, but the enclosed volume is unconstrained, *i.e.*, the membrane is assumed to be permeable on the experimental time scale. The vesicle interacts with a solid substrate *via* a potential $V(z)$, where z denotes the distance from the substrate. $z = 0$ denotes the position of the minimum of $V(z)$. As illustrated in Fig. 2, we parameterize the vesicle shape by the tangent angle, $\psi(s)$, as a function of the contour length, $0 \leq s < L_s$.[13,41,42]

For the numerical minimization of the vesicle (free) energy, we expand $\psi(s)$ around a spherical vesicle in a Fourier series[42,43]

$$\psi(s) = \frac{\pi}{L_s}s + \sum_{k=0}^{N_{\max}} a_k \sin\left(\frac{\pi[k+1]}{L_s}s\right) \tag{4}$$

In the absence of substrate or volume interactions, the vesicle shape is spherical. Its radius, R_0, is set by the membrane area, $L_s = \pi R_0$, and $a_k = 0$ for all $k = 0,\ldots,N_{\max} - 1$. This parameterization fulfills the boundary condition, $\psi(0) = 0$ and $\psi(L_s) = \pi$. The arc length, L_s, must be chosen such that $r(L_s) = 0$.

The position of the axially symmetric vesicle membrane takes the form

$$r(s) = \int_0^s \mathrm{d}s' \cos(\psi(s')) \tag{5}$$

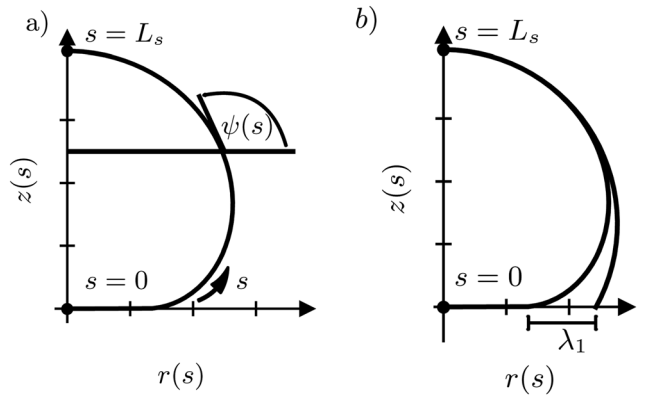

Fig. 2 (a) Parameterization of an axially symmetric vesicle. The arc-length parameter, $0 \leq s < L_s$, runs from the bottom center, $z(s = 0) = z_0$, $r(s = 0) = 0$, to the top $z(s = L_s) = H$, $r(s = L_s) = 0$. The angle, $\psi(s)$, denotes the angle between the tangent of the vesicle's contour and the horizontal. (b) Comparison between the vesicle shape, parameterized by $\psi(s)$, z_0, L_s, and a spherical cap. The length, λ_1, is the distance between the contact radius of the spherical cap and that of the vesicle.

$$z(s) = z_0 + \int_0^s \mathrm{d}s' \sin(\psi(s')) \tag{6}$$

where the position, z_0, at the bottom center specifies the position of the vesicle along the symmetry axis. Thus, the vesicle shape and position are specified by z_0, L_s, and the Fourier coefficients a_k with $k = 0,\ldots,N_{\max} - 1$ of $\psi(s)$, obeying the constraint $r(L_s) = 0$.

2.3.2 The energy of the vesicle – bending *vs.* adhesion. The energy of the vesicle is comprised of three contributions: bending energy,[15] interaction with the substrate,[12,13,39,41] and buoyancy.[40] In the following, we ignore the latter aspect.

We represent the bending energy by the Helfrich Hamiltonian, $\mathscr{H}_b$, that expresses the energy costs *via* a surface integral over the two principal curvatures, C_1 and C_2.[15] Using the parameterization, $\psi(s)$, these curvatures take the form[13,41,42]

$$C_1(s) = \frac{\mathrm{d}\psi}{\mathrm{d}s} = \frac{\pi}{L_s} + \sum_{k=0}^{N_{\max}} a_k \frac{\pi[k+1]}{L_s}\cos\left(\frac{\pi[k+1]}{L_s}s\right) \tag{7}$$

$$C_2(s) = \frac{\sin(\psi(s))}{r(s)} \tag{8}$$

Since the two membrane leaflets are symmetric, the spontaneous curvature of the bilayer membrane vanishes. Likewise, we have assumed that the membrane is homogeneous and its topology fixed such that the Gaussian curvature term only provides a constant contribution and needs not to be considered. Thus the bending energy takes the simple form[13,41,42]

$$\mathscr{H}_b = \frac{\kappa}{2}\int_0^{L_s} \mathrm{d}s\, 2\pi r\left(\frac{\mathrm{d}\psi}{\mathrm{d}s} + \frac{\sin(\psi)}{r}\right)^2 \tag{9}$$

The parameter, κ, denotes the bending energy of the membrane, and it sets the energy scale. The integration of $\mathscr{H}_b$ and subsequent quantities is performed numerically in the zr-plane by discretizing the parametric vesicle shape, $r(s)$, $z(s)$ into N_s points. Using a trapezoidal integration, the error is on the order ${N_s}^{-2}$.

Whereas prior studies often modeled the interaction between vesicle membrane and substrate per unit area by a contact potential[12,13,41] (see ref. 39 for an exception), we consider short-range potentials, $V_c(z)$, with a finite width, σ_w, and long-range potentials, $V_w(z)$, that represent van der Waals interactions. The two types of potentials are illustrated in Fig. 3. The origin of the z-axis is the minimum of the membrane–substrate potential, and $-\Delta\gamma_w$ denotes the value of the membrane–substrate potential at its minimum. The short-range potential is given by

$$V_c(z) = \begin{cases} -4\Delta\gamma_w\left(\dfrac{z}{\sigma_w} + \dfrac{1}{2}\right) & \text{for} \quad z < -\dfrac{\sigma_w}{2} \\ -\Delta\gamma_w\left(1 - \dfrac{2z}{\sigma_w}\right)\left(1 + \dfrac{2z}{\sigma_w}\right) & \text{for} \quad |z| < \dfrac{\sigma_w}{2} \\ 0 & \text{otherwise} \end{cases} \tag{10}$$

and the long-range interaction takes the Hamaker-form

$$V_w(z) = \frac{3\sqrt{3}}{2}\Delta\gamma_w\left(\mathrm{sign}(\Delta\gamma_w)\left[\frac{\sigma_w}{z + z_w}\right]^9 - \left[\frac{\sigma_w}{z + z_w}\right]^3\right) \tag{11}$$

where the sign-function assures that potential remains repulsive

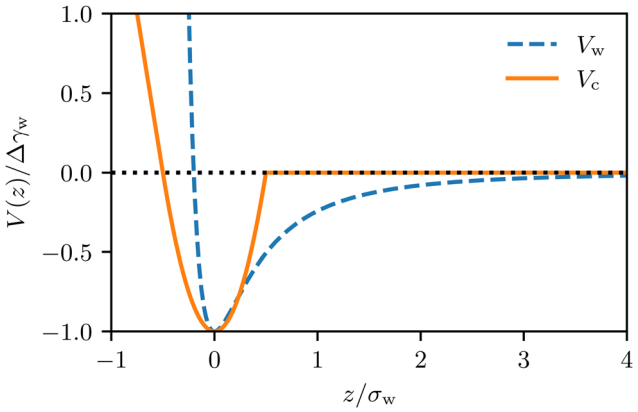

Fig. 3 Illustration of the long-range and short-range membrane–substrate interactions, $V_w(z)$ and $V_c(z)$, according to eqn (10) and (11).

even for $\Delta\gamma_w < 0$. $z_w = \sqrt[6]{3}\sigma_w$ shifts the minimum of $V_w(z)$ to $z = 0$. We note that the long-range power-law decay is scale-free.

Integrating the membrane–substrate interaction over the vesicle, we obtain the adhesion energy

$$\mathscr{H}_w = \int_0^{L_s} \mathrm{d}s\, 2\pi r(s) V(z(s)) \tag{12}$$

Instead of characterizing the range of the potential by σ_w, we can use the curvature, V'', of the potential at its minimum. The latter quantity controls the experimentally accessible, thermal height fluctuations of a membrane, bound to the substrate (*cf.* Section 3.3). For the two types of potential, we respectively obtain

$$V'' \equiv \left.\frac{\mathrm{d}^2 V_c}{\mathrm{d}z^2}\right|_{z=0} = -8\frac{\Delta\gamma_w}{{\sigma_w}^2} \tag{13}$$

$$\left.\frac{\mathrm{d}^2 V_w}{\mathrm{d}z^2}\right|_{z=0} = 9\sqrt[6]{81}\frac{\Delta\gamma_w}{{\sigma_w}^2} \tag{14}$$

2.3.3 Restraints. In the following we seek to minimize the vesicle energy, $\mathscr{H}_0[\psi,z_0,L_s] \equiv \mathscr{H}_b + \mathscr{H}_w$, under the following constraints: (i) fixed membrane area, $A[\psi] = 4\pi{R_0}^2$ and (ii) vesicle closure, $r(L_s) = 0$. Additionally, we could enforce (iii) the volume, V_0, enclosed by the vesicle. Numerically, the constraints are mollified, and the resulting restraints are incorporated into the energy functional *via* umbrella potentials with large spring constants.

Deviations of the membrane area, $A[\psi,L_s]$, from the reference value, $A_0 = 4\pi{R_0}^2$, increase the energy by an amount

$$H_A = \frac{k_A}{2}\left(A[\psi,L_s] - 4\pi{R_0}^2\right)^2 \tag{15}$$

with

$$A[\psi,L_s] = \int_0^{L_s} \mathrm{d}s\, 2\pi r(s) \tag{16}$$

From the deviations, we can estimate the membrane tension

$$\gamma = k_A(A[\psi,L_s] - 4\pi{R_0}^2) \tag{17}$$

in the large k_A-limit, *i.e.*, k_A is related to the inverse areal compressibility of the membrane.

Likewise, vesicle closure, $r(L_s) = 0$, gives rise to the contribution

$$H_r = \frac{k_r}{2}(r(L_s))^2 \tag{18}$$

For completeness, we mention that deviations of the enclosed volume $V[\psi,L_s] = \int_0^{L_s}\mathrm{d}s\,\sin(\psi)\,\pi r^2$ from a reference value, V_0, could be penalized by an energy contribution

$$H_V = \frac{k_V}{2}(V[\psi,L_s] - V_0)^2 \tag{19}$$

yielding the pressure difference ($\Delta P = k_V(V[\psi,L_s] - V_0)$ across the membrane for $k_V \to \infty$. In the following, however, we set $k_V = 0$ and let the vesicle's volume adjust.

The total energy, $\mathscr{H} = \mathscr{H}_0 + \delta H$, to be minimized contains the bending and adhesion energies, and the restraints, $\delta H = H_A + H_r + H_V$. In the following, we measure all energies in units of the membrane's bending rigidity, κ, and all length scales in units of the radius, R_0, of a spherical vesicle with the same membrane area as the restraint, A_0.

$$\begin{aligned}\frac{\mathscr{H}[\psi,z_0,L_s]}{\kappa} &= \pi\int_0^{L_s}\frac{\mathrm{d}s}{R_0}\frac{r}{R_0}\left(R_0\frac{\mathrm{d}\psi}{\mathrm{d}s} + R_0\frac{\sin(\psi)}{r}\right)^2 \\ &+ \underbrace{\frac{\Delta\gamma_w {R_0}^2}{\kappa}}_{\equiv\tilde{\varepsilon}_w}\int_0^{L_s}\frac{\mathrm{d}s}{R_0}\frac{2\pi r}{R_0}\frac{V_w(z)}{\Delta\gamma_w} \\ &+ \frac{k_A {R_0}^4}{2\kappa}\left(\frac{A[\psi,L_s]}{{R_0}^2} - 4\pi\right)^2 \\ &+ \frac{k_r {R_0}^2}{2\kappa}\left(\frac{r[\psi,L_s](L_s)}{R_0}\right)^2 \\ &+ \frac{k_V {R_0}^6}{2\kappa}\left(\frac{V[\psi,L_s] - V_0}{{R_0}^3}\right)^2\end{aligned} \tag{20}$$

The thermodynamic state of the vesicle in contact with a solid substrate is characterized by the dimensionless parameter combinations, $\tilde{\varepsilon}_w = \frac{\Delta\gamma_w {R_0}^2}{\kappa}$ (ref. 12 and 13) that measures the relative strength of adhesion with respect to the bending energy. As a consequence, we can vary this dimensionless characteristic by changing the vesicle size, R_0, without altering the membrane–substrate interaction, $V(z)$.

The energy functional, $\mathscr{H}$, is numerically minimized with respect to ψ, z_0, L_s by a conjugate-gradient method. Typical parameter values are compiled in Table 1. The values that minimize $\mathscr{H}[\psi,z_0,L_s]$ are denoted by ψ^*, L_s^*, z_0^*; these values depend on the thermodynamic state, specified by $\tilde{\varepsilon}_w$. Inserting these values into the energy functional, we obtain the energy, $H = \mathscr{H}[\psi^*, L_s^*, z_0^*]$ of the vesicle at a given thermodynamic state. Note that this procedure completely ignores thermal fluctuations.

To study the adhesion transition we quantify the dimensionless energy difference between the vesicles in contact with a

Table 1 Compilation of typical parameters for the numerical minimization of the vesicle shape

Variable	Value
N_{max}	128, 144
N_s	288, 578, 2048
σ_w/R_0	0.03, 0.01 or 0.002
$\tilde{k}_A \equiv k_A R_0^4/\kappa$	100
$\tilde{k}_V \equiv k_V R_0^6/\kappa$	0, permeable membrane
$\tilde{k}_r \equiv k_r R_0^2/\kappa$	1000

substrate and a free, unbound vesicle $H = 8\pi\kappa$

$$\tilde{f} = \frac{\mathscr{H}_0[\psi^*, L_s^*, z_0^*]}{8\pi\kappa} - 1 \qquad (21)$$

3 Results

3.1 Validity of the transversality condition for finite-ranged membrane–substrate interaction

Fig. 4a presents the vesicle shape for long-range interaction, V_w, with $\sigma_w = 0.002R_0$ and various adhesion strengths, $\tilde{\varepsilon}_w$. Upon increasing $\tilde{\varepsilon}_w$, the vesicle gradually spreads on the substrate. As shown in Fig. 4b, the confocal side views of vesicles in the absence (green) and presence (red) of attractive interactions qualitatively exhibit good agreement.

For small $\tilde{\varepsilon}_w = 1$ – the pinned state[39] – the vesicle shape is very close to a sphere, yet the vesicle benefits from the long-range attraction. We note that the second-order wetting transition for zero-ranged interactions at $\tilde{\varepsilon}_{wc} = 2$ is rounded. Instead, the thermodynamic transition is a first-order and occurs at $\tilde{\varepsilon}_w = 0$ for $\sigma_w > 0$ (*vide infra*).

Fig. 4c depicts a detail of the vesicle shape in the contact zone, where one can appreciate a small dent at the edge of the adhesion zone. Such a nonmonotonic behavior of the distance, $z(s)$, between membrane and substrate results from the simultaneous optimization of the adhesion energy and bending energy. The width of this dent increases with σ_w. Vertical lines at the axis indicate the geometric radius of the contact area, extracted from the maximum of the first principal curvature. One can observe that both, the location of the dent and the maximal curvature, provide a rather faithful estimate of the edge of the adhesion zone.

The first principal curvature, $C_1(s)$, along the vesicle is shown in Fig. 4d. For a contact potential, $\sigma_w \to 0$, the curvature jumps from 0 inside the contact zone to a finite value that is dictated by the transversality condition[12,13]

$$(C_{1max}R_0)^2 = 2\tilde{\varepsilon}_w \quad \text{for contact interactions} \qquad (22)$$

This boundary condition at the edge of the contact zone relates the membrane geometry, C_1, to the thermodynamic strength of adhesion, $\tilde{\varepsilon}_w$. For $\sigma_w > 0$, there is no jump singularity of C_1 but the curvature exhibits a rapid, sigmoidal variation at the edge of the adhesion zone. For potentials, V, with a nonzero interaction range, Evans suggested using the maximal curvature, C_{1max}, instead of the contact curvature in the transversality condition.[51] Note that the transversality condition systematically underestimates the maximal curvature. Panel (d) of Fig. 4

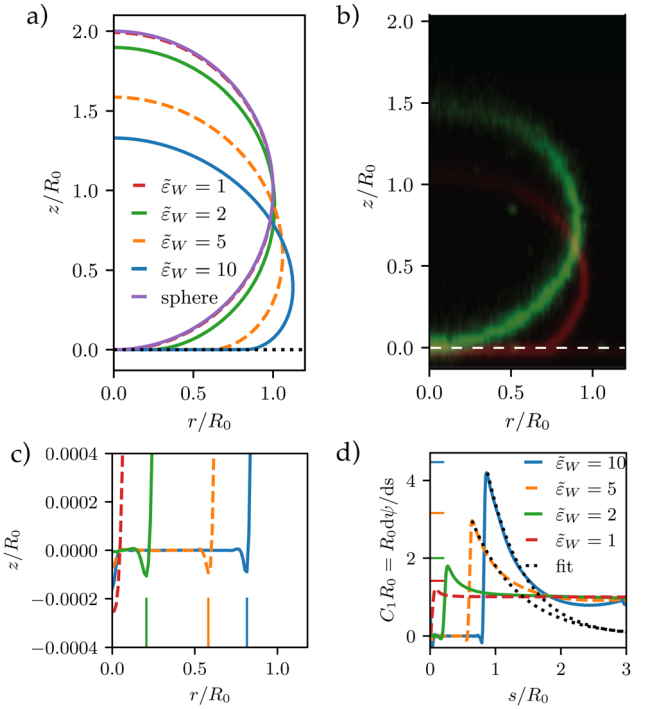

Fig. 4 Vesicle shape for long-range interactions. (a) Shape of the axially symmetric vesicle, $r(s)$, $z(s)$, for various $\tilde{\varepsilon}_w$ as indicated in the key and comparison to a spherical vesicle. (b) Vesicle shapes obtained in the absence (green) and presence (red) of attractive interactions by experiments showing the same qualitative tendency. (c) Detail of the vesicle shape at the edge of the adhesion zone, exhibiting a dent, *i.e.*, a ring with $z(s) < 0$. The vertical lines mark the geometric radius of the contact zone, eqn (25), obtained by the position of maximal curvature. (d) First principal curvature, $C_1(s) = \frac{d\psi}{ds}$, as a function of the arc-length parameter, s. Note the negative values of the curvature at the edge of the adhesion zone. The lines at the ordinate axis indicate the maximal-curvature estimate, $C_{1max}R_0 = \sqrt{2\tilde{\varepsilon}_w}$, according to the transversality condition, eqn (22). (The dotted line presents fits, $C_1(s) = C_{1max}\exp(-[s - s_{max}]/\lambda_E)$ beyond the maximum at s_{max}, analog to eqn (31).)

reveals that the dent at the edge of the adhesion zone gives rise to negative C_1-values. Thus, the jump in C_1 that emerges in the limit $\sigma_w \to 0$ can alternatively be estimated by the change, $\Delta C_1 \equiv C_{1max} - C_{1min}$, of curvature at the edge of the adhesion zone.

To further study the effects of the long-range potential, we observed the contact area of the adsorbed vesicle. There is no singularity at the edge of the adhesion zone but the vesicle shape gradually detaches from the substrate (*vide infra*). We can define a thermodynamic contact area *via* the first derivative of the energy, $H = \mathscr{H}[\psi^*, z_0^*, L_s^*]$, with respect to the adhesion strength, $\Delta\gamma_w$.

$$\frac{\partial H}{\partial \Delta\gamma_w} = \frac{\mathscr{H}_w}{\Delta\gamma_w} + \int_0^{L_s} ds \underbrace{\left.\frac{\delta\mathscr{H}[\psi, z_0, L_s]}{\delta\psi}\right|_*}_{=0} \frac{\partial\psi^*(s)}{\partial\Delta\gamma_w} + \left.\frac{\partial\mathscr{H}}{\partial z_0}\right|_* \frac{\partial z_0^*}{\partial\Delta\gamma_w} + \left.\frac{\partial\mathscr{H}}{\partial L_s}\right|_* \frac{\partial L_s^*}{\partial\Delta\gamma_w} \qquad (23)$$

$$\tilde{A}_w^{th} \equiv \frac{A_w^{th}}{R_0^2} = \frac{1}{R_0^2}\frac{\partial H}{\partial\Delta\gamma_w} = \frac{\mathscr{H}_w/\kappa}{\tilde{\varepsilon}_w} \qquad (24)$$

Alternatively, we can geometrically identify the radius, r_c^{geo}, of the contact zone by the location of the maximum curvature, $C_1(s) = d\psi/ds$

$$r_c^{geo} = r(\arg\max_s d\psi/ds) \quad (25)$$

and obtain a geometric area of the contact zone

$$\tilde{A}_w^{geo} = \frac{\pi\left(r_c^{geo}\right)^2}{R_0^2} \quad (26)$$

These estimates of the contact area, according to eqn (24) (solid lines, open symbols) and eqn (26) are shown in Fig. 5a. Both definitions exhibit qualitatively similar behaviors but $\tilde{A}_c^{geo}$ is slightly but consistently larger than $\tilde{A}_c^{th}$. The so-defined contact area continuously increases with $\tilde{\varepsilon}_w$, and it approaches a constant value for $\tilde{\varepsilon}_w \to 0$ in the pinned state, where the vesicle benefits from the potential but is hardly deformed. For a repulsive substrate, $\tilde{\varepsilon}_w < 0$, the vesicle is unbound and the contact area vanishes. The discontinuity of the contact area at $\tilde{\varepsilon}_w = 0$ marks the first-order adhesion transition. This behavior differs significantly from the second-order transition at $\tilde{\varepsilon}_w = 2$ predicted for a contact potential behavior.[12,13]

Thus, it is warranted to validate the transversality condition, eqn (22), for finite interaction ranges, $\sigma_w > 0$. In Fig. 5b, we explore the influence of the finite potential range on the transversality condition. We observe, that the linear relation between $\tilde{\varepsilon}_w$ and $(C_{1max}R_0)^2$ remains valid, however, the slope and offset are specific to the details of the membrane–substrate interaction

$$(C_{1max}R_0)^2 \approx \Gamma\tilde{\varepsilon}_w + \Delta \quad (27)$$

As shown in the inset of panel (b), the slope, Γ, approaches its asymptotic value 2[12,13] for $\sigma_w/R_0 \to 0$ from below. A correction of the form $(\sigma_w/R_0)^\alpha$ describes the data. For the range of σ_w/R_0 studied, the exponent adopts a value close to 1/3. Thus, for larger σ_w/R_0, the maximum curvature increases less quickly with increasing $\tilde{\varepsilon}_w$ because the vesicle profits still from the potential at some distance and hence large curvatures are energetically not favorable.

For the large vesicles used in the experiment, $\sigma_w/R_0 \ll 1$, however, the slope, Γ, is close to 2 and we use eqn (22) to calculate the adhesion free energy, $\Delta\gamma_w$.

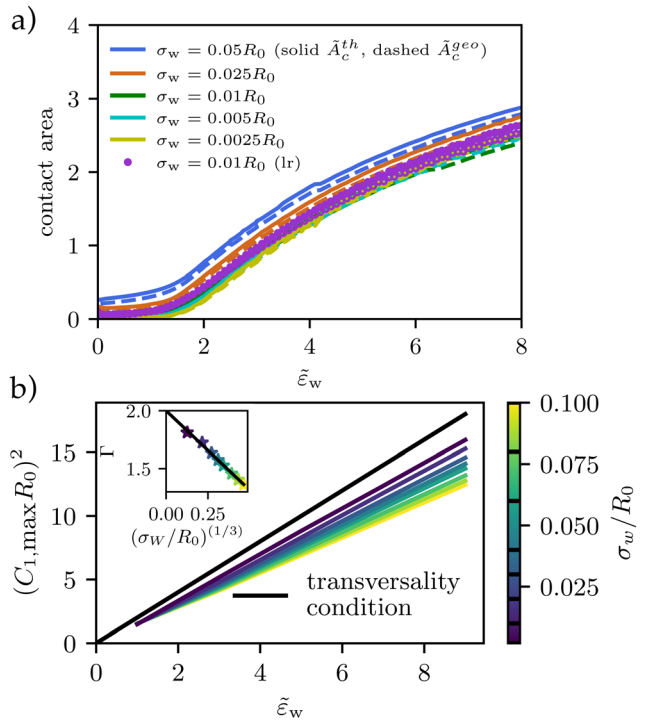

Fig. 5 Vesicle shape for long-range potential, V_w, with scale $\sigma_w = 0.002R_0$ as a function of adhesion strength, $\tilde{\varepsilon}_w$ as indicated in the key. (a) Thermodynamic and geometric contact area, $\tilde{A}_c^{th}$, and $\tilde{A}_c^{geo}$, as a function of adhesion strength, $\tilde{\varepsilon}_w$, for short-range and long-range potentials of varying width, σ_w. (b) For potentials approaching a contact potential, the transversality condition is met. For wider potentials, the curvature increases slower with increasing adhesion strength (compare eqn (27)). As shown in the inset, Γ decreases from 2 with $(\sigma_w/R_0)^{(1/3)}$.

3.2 Characterization of switchable substrates coated with stimulus-responsive polymer brushes

PAA-Cys5-biotin brushes were grafted on the surface of DOPC membranes deposited on planar solid substrates (supported membranes) doped with 2 mol% DOPE-biotin neutravidin crosslinkers. The supported membranes were prepared by the fusion of small unilamellar vesicles (*cf.* Section 2.2.1). The major advantage of supported membranes over the commonly used, direct grafting of polymers onto solid substrates *via* covalent bonds (called "grafting onto" method) is their capability to achieve high and well-defined grafting densities. As DOPC and DOPE-biotin are miscible, the average grafting distance $\langle d\rangle$ can be controlled at nm accuracy simply by the molar fraction of DOPE-biotin χ_{biotin}, $\langle d\rangle = (0.6/\chi_{biotin})^{0.5}$ [nm], assuming the area per lipid molecule is 0.6 nm^2.[52] As schematically shown in Fig. 6a, our previous study using quartz crystal microbalance with dissipation suggested that the binding of Cd^{2+} ions to PAA-Cys5 leads to the compaction of brushes. High-energy X-ray reflectivity experiments were performed to verify the structural changes of PAA-Cys5 brushes. Note that the use of high energy (17.48 keV from Mo Kα) was necessary to guarantee the sufficiently high transmittance of X-ray beam through bulk water.[53,54] Fig. 6b shows the X-ray reflectivity data and the best fit results (solid lines, Fig. 6b). Fig. 6c shows the scattering length density (SLD) profiles reconstructed from the best fit model (upper panel) and the correspondence to the layer structure (lower panel). The addition of 1 mM Cd^{2+} ions caused a clear change in the global shape of the X-ray reflectivity (Fig. 6b), suggesting that PAA-Cys5-biotin brushes change their conformation. The layer parameters obtained from the best fit results (Table 2) and the magnified SLD profiles in the vicinity of the interface (Fig. 6c, inset) suggest that the brush layer thickness decreased from d_0 = 14.3 nm to d_{Cd} = 10.3 nm, accompanied by the decrease in the brush/solution interface roughness from σ_0 = 2.0 nm to σ_{Cd} = 1.2 nm. The obtained results indicate that PAA-Cys5-biotin brushes become more compact in the presence of 1 mM Cd^{2+} ions, resulting in a sharper transition from the brush region to the

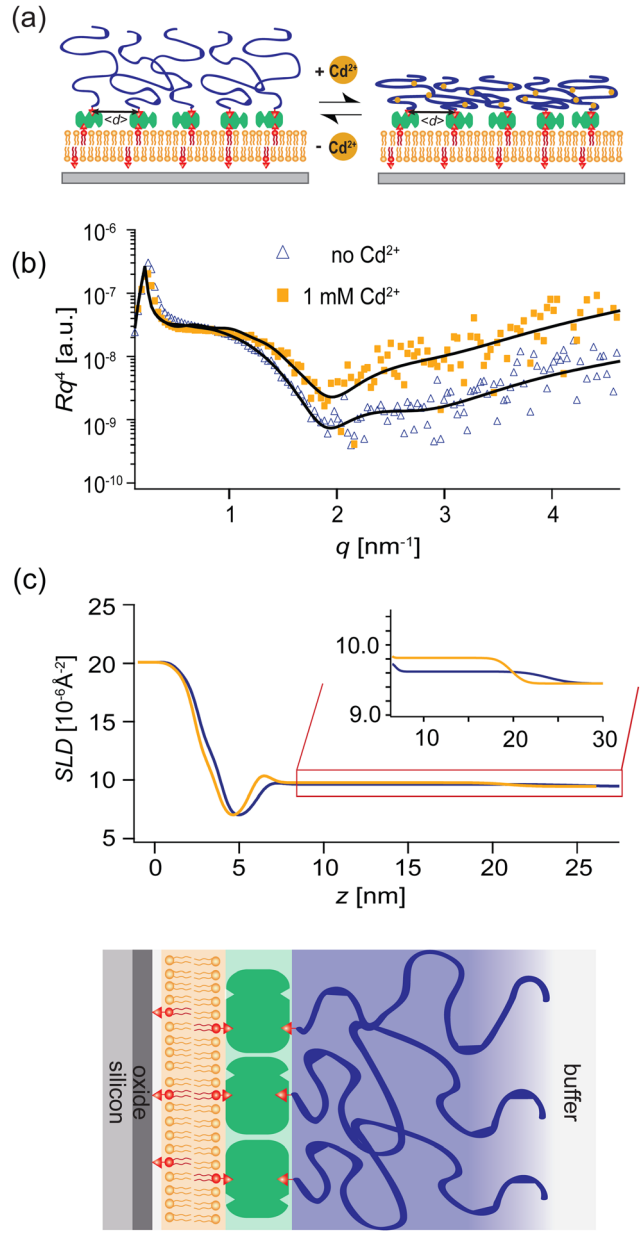

Fig. 6 Stimulus responsive polymer brushes as "switchable substrates". (a) Grafting of PAA-Cys5-biotin onto a substrate coated with a supported lipid membrane, displaying neutravidin anchors that are separated at $\langle d \rangle \approx 6$ nm. The binding of Cd^{2+} ions to –COOH and –SH groups leads to the compaction of brushes. (b) High energy specular X-ray reflectivity data for the PAA-Cys5-coated substrate in the absence (blue) and presence (yellow) of 1 mM $CdCl_2$. A distinct change caused by 1 mM $CdCl_2$ suggests the thickness decrease and the density increase. (c) Scattering length density profiles of the PAA-Cys5-coated substrate calculated from the best fit models (solid lines in panel b), verifying the compaction of PAA-Cys5 in the presence of Cd^{2+} ions.

bulk solution (Fig. 6a). The compaction of PAA-Cys5-biotin caused by additional Cd^{2+} ions suggests that the negative charges carried by –COOH side chains were compensated by the binding of Cd^{2+} ions.[55] In fact, the zeta potential of PAA-Cys5-biotin brushes grafted on supported membranes deposited on SiO_2 microparticles (radius: 1.5 μm) showed a monotonic increase from $\zeta_{1\mu M} = -26$ mV to $\zeta_{1mM} = -10$ mV.[55] This qualitatively agrees well with previous reports, showing that the decrease in the ionization degree of side chains results in the compaction of polyelectrolyte brushes.[32] It should be noted that the addition of 1 mM Cd^{2+} ions does not alter the pH (7.4) or Debye screening length ($\kappa_D^{-1} < 10$ Å) because the solution contains 100 mM NaCl buffered with 10 mM Tris (pH 7.4). In fact, Yamamoto *et al.* systematically varied the side chain moieties and demonstrated that not only –COOH groups but also the coexistence of –SH groups are necessary to achieve the sensitive capture of Cd^{2+} ions.[33] Further spectroscopic studies, under the systematic variations of the side chain functionalities, will help us understand the molecular-level mechanism of interactions between Cd^{2+} ions and PAA-Cys5.

3.3 Experimental modulation of wetting by lipid vesicles

Panels (a and b) of Fig. 7 schematically show a "non-wetting vesicle" hovering on the brush-coated substrate and a "wetting vesicle" establishing a stable adhesion contact to the brush-coated substrate, respectively. To judge whether the vesicle established a stable adhesion contact or not, we visualized the DOPC vesicles by reflection interference contrast microscopy (RICM) from below at $[CdCl_2] = 0$ mM, 0.25 mM and 1.0 mM, *cf.* Fig. 7(c–e). In addition, the global shape of the vesicle was reconstructed from the confocal fluorescence microscopy images, and the cross-sectional side view was extracted by slicing the vesicle in the middle plane (Fig. 7f–h). Here, the density of liquid inside was adjusted to be slightly higher than the buffer outside ($\Delta\rho = 40$ kg m^{-3}) in order that the vesicles sediment towards the substrate surface.

The RICM image taken in the absence of Cd^{2+} ions showed a faint dark spot at the center of a bright disk, whose intensity fluctuates over time. This indicates that the vesicle sediments due to the density difference but does not adhere onto the substrate.[21,49] In fact, the side view of the vesicle reconstructed from the confocal image stacks shows no sign of wetting (Fig. 7f).

Table 2 Layer parameters of PAA-Cys5 corresponding to the best fit results of high energy specular X-ray reflectivity data (Fig. 6b, solid lines)

PAA-Cys5-biotin in the absence of Cd^{2+}			
	d (nm)	SLD (10^{-6} Å^{-2})	σ (nm)
SiO_2	1.23 ± 0.03	18.9	0.55 ± 0.01
Buffer	0.46 ± 0.01	9.45	0.45 ± 0.02
Lipid headgroup$_{inner}$	0.68 ± 0.01	13.1 ± 0.2	0.47 ± 0.01
Lipid alkylchain	2.24 ± 0.03	6.8 ± 0.01	0.59 ± 0.02
Lipid headgroup$_{outer}$	0.89 ± 0.05	12.3 ± 0.2	0.62 ± 0.06
Neutravidin^{+} PAA-Cys5-biotin	18.2 ± 0.8	9.7 ± 0.1	2.05 ± 0.1
PAA-Cys5-biotin in the presence of 1 mM Cd^{2+}			
	d (nm)	SLD (10^{-6} Å^{-2})	σ (nm)
SiO_2	1.19 ± 0.04	18.9	0.51 ± 0.01
Buffer	0.48 ± 0.01	9.45	0.44 ± 0.03
Lipid headgroup$_{inner}$	0.67 ± 0.02	12.9 ± 0.3	0.44 ± 0.03
Lipid alkylchain	2.21 ± 0.04	7.1 ± 0.02	0.59 ± 0.03
Lipid headgroup$_{outer}$	0.88 ± 0.07	12.3 ± 0.4	0.57 ± 0.06
Neutravidin^{+} PAA-Cys5-biotin	14.2 ± 1.2	9.9 ± 0.1	1.20 ± 0.11

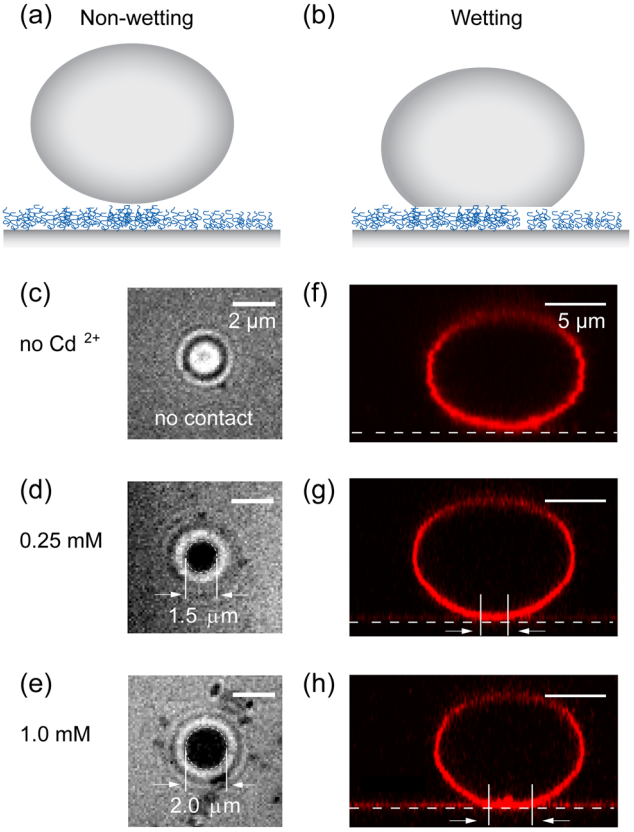

Fig. 7 Modulation of wetting of PAA-Cys5 substrate by giant lipid vesicles ($\Phi \approx 10$ μm) by Cd^{2+} ion concentration. Schematic illustration of (a) non-wetting and (b) wetting vesicles. Reflection interference contrast microscopy (RICM) images (c–e) and side views of vesicles reconstructed from confocal microscopy images (f–h) of DOPC vesicles at $[CdCl_2]$ = 0 mM (c), 0.25 mM (d), and 1.0 mM (e). The first sign of wetting was observed at $[CdCl_2]$ = 0.25 mM, which can be identified by the formation of a stable, dark adhesion zone in the middle of the interferometric image.

In contrast, the RICM image of a vesicle taken at $[CdCl_2]$ = 0.25 mM shows a stable dark disk due to the destructive interference (Fig. 7d). This suggests that the vesicle establishes a stable adhesion/wetting contact to the brush-coated substrate. Notably, the formation of a flat vesicle-substrate contact can hardly be detected from the confocal side view (Fig. 7g). When we increased the concentration of Cd^{2+} ions, the wetting of brush-coated substrate with lipid vesicles became more pronounced, which can be characterized by a large adhesion contact (Fig. 7e) and a clear flattening of the bottom (Fig. 7h). By screening Cd^{2+} ion concentration systematically, we verified that the adhesion contact can be detected only at $[CdCl_2] \geq 0.25$ mM. To verify the reproducibility of our experimental finding, several sets of confocal (Fig. S1, ESI†) and RICM (Fig. S2, ESI†) are presented in ESI.† These data demonstrated that RICM is very sensitive to detecting the onset of "(partial) wetting" of soft substrates by lipid vesicles, which can hardly be detected by the confocal side view.

Previously, Nardi *et al.* showed the change in vesicle-substrate interactions by using vesicles incorporating cationic lipids interacting with supported membranes doped with negatively charged lipids.[56] The pH modulation caused changes in the surface charge density, where they observed the breakdown of Young–Dupré-type wetting by the formation of the three-dimensional protrusion (blisters). In contrast the confocal images of lipid vesicles indicated that the vesicles showed no sign of adhesion on lipid membranes with no PAA-Cys5 brushes, independent of the presence or absence of 1 mM Cd^{2+} ions (Fig. S3, ESI†). This could be attributed to the fact that our experiments were performed in the presence of 10 mM Tris buffer, which is much milder than the conditions used in the previous report of Lis *et al.*[57] As shown in Fig. 6, our PAA-Cys5-coated substrates showed a clear change in the thickness and roughness by a slight change in Cd^{2+} ion concentration in 100 mM NaCl buffered with 10 mM Tris. This enables us to modulate the "wetting" state of vesicles without changing pH or electrochemical screening. Furthermore, as demonstrated in our previous study, PAA-Cys5 brushes, possessing both –SH and –COOH side chains like naturally occurring phytochelatin and metallothionein proteins,[58,59] selectively react to a subtle change in $[CdCl_2]$.[55] As the switching of PAA-Cys5 brushes does not require any temperature changes, such as poly(*N*-isopropylacrylamide) (PNIPAAm) brushes,[60] PAA-Cys5 brushes allow to avoid hydrodynamic perturbation by thermal convection.

3.4 Determination of adhesion-free energy from experimental data

Fig. 8a shows a typical RICM image of a DOPC vesicle adhered on a PAA-Cys5-coated substrate. To gain high counting statistics, the signal intensity was radially integrated over azimuth angle ϕ (Fig. 8b). The height profile shown in Fig. 8c was reconstructed by an inverse cosine transformation of the radially integrated RICM signal intensity (Fig. 8b).[14] What differentiates the wetting by lipid vesicles from that by a droplet of a simple fluid is that the height profile of the membrane in the vicinity of the substrate is dominated by the bending elasticity. On larger scales, the global shape of vesicles is governed by the geometry-dependent membrane tension, γ. The transition from the elasticity-dependent height profile to the tension-dominated vesicle profile occurs on the scale of the capillary length,[14,61,62]

$$\lambda_\gamma = \sqrt{\frac{\kappa}{\gamma}} \tag{28}$$

For zero-ranged, contact interaction between membrane and substrate, the minimization of the vesicle energy in Monge representation,[41,61]

$$\lambda_\gamma{}^2 \nabla^4 z - \nabla^2 z = 0 \tag{29}$$

i.e., λ_γ sets the scale of the profile in the vicinity of the substrate. Bruinsma wrote down a one-dimensional solution[62] that fulfills the boundary conditions, $z = 0$, $dz/dr = 0$, and $C_{1\max} = d^2z/dr^2 = \alpha/\lambda_E$ at the edge of the adhesion zone, $r = r_E$.§

§ Note that the fourth solution, e^{r/λ_E}, for the one-dimensional problem is not used. The corresponding solution with axial symmetry

$$\frac{z(r)}{\lambda_E} = C_{1\max}\lambda_E\left\{\frac{K_0(r/\lambda_E)}{K_0(r_E/\lambda_E)} - 1 + \frac{K_1(r_E/\lambda_E)\, r_E}{K_0(r_E/\lambda_E)\,\lambda_E}\ln\frac{r}{r_E}\right\}$$

has been given in ref. 61, where K_n denotes the nth modified Bessel functions of second kind. The modified Bessel function of first kind, $I_0(r/\lambda_E)$, can additionally be used to construct a solution.

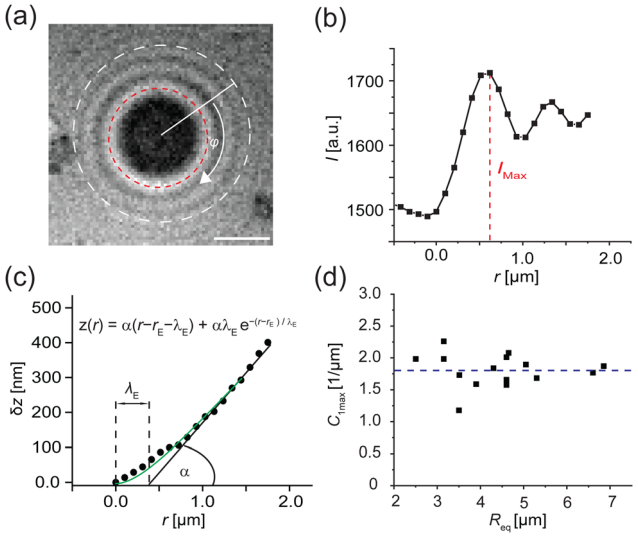

Fig. 8 Determination of adhesion free energy $\Delta\gamma_W$ at $[CdCl_2]$ = 1 mM. (a) A typical RICM image of a vesicle adhered on a PAA-Cys5-coated substrate at $[CdCl_2]$ = 1 mM. Scale bar: 2 μm. (b) Radially integrated RICM signal intensity *versus* distance from the center. The line coincides with the fitting with eqn (30). (c) Membrane height z *versus* the distance r, reconstructed from the fitting shown in panel (b). (d) Contact curvature C_{1max} plotted *versus* the radius of each vesicle at the plane of equator R_{eq}.

$$z(r) = \alpha(r - r_E - \lambda_E) + \alpha\lambda_E e^{-(r-r_E)/\lambda_E} \quad (30)$$

The parameter, λ_E, coincides with the capillary length, λ_γ, by assuming that the fit is restricted to the vicinity of the edge of the adhesion zone and the adhesion is sufficiently strong, $|\nabla z| \ll 1$ and $r_E/\lambda_\gamma \gg 1$, respectively. This expression has been employed to analyze experimental data,[20,21] yielding the effective contact angle, α, and the length scale, λ_E.

Within the Monge representation, $s \approx r$, and eqn (30) yields for the curvature,

$$C_1(r) \approx \frac{d^2z}{dr^2} = \frac{\alpha}{\lambda_E}\exp\left(-\frac{r - r_E}{\lambda_E}\right) \quad (31)$$

for $r > r_E$. Indeed, we qualitatively observe in Fig. 4a that the curvature, $C_1(s)$, decays the faster (*i.e.*, smaller λ_γ and larger γ, see Fig. 9b) the stronger the adhesion, $\tilde{\varepsilon}_w$, is. For larger s, however, the Monge representation becomes inappropriate and $C_1(s)$ does not decay to zero but to a constant value that characterizes the cap-shaped, upper half of the vesicle, *i.e.*, eqn (30) fails to capture the tension-dominated, cap shape of the vesicle profile far away from the edge of the adhesion zone, $(r - r_E)/\lambda_E \gg 1$.

In Fig. 9, we systematically investigate the two geometric estimates of the capillary length – λ_1 as depicted in Fig. 2b and λ_E obtained by fitting eqn (31) – and compare these data with the definition, λ_γ, according to eqn (28).

For λ_1, we consider the 18% of the data closest to $s = L_s$ and fit a sphere. This spherical cap is characterized by its radius, R_{cap}, and the height of the top, $z(L_s)$. Given the radius, r_E, of the edge of the adhesion zone, λ_1, is obtained.

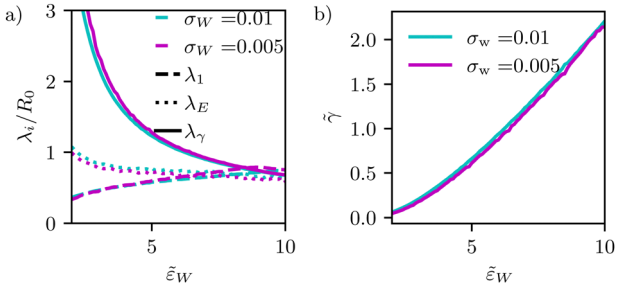

Fig. 9 (a) Dependence of different estimates of capillary length – λ_γ according to eqn (28), the extrapolation length λ_1 from a cap-shape approximation (see Fig. 2b), and the length λ_E extracted from the height profile in the ultimate vicinity of the edge of the adhesion zone – on the adhesion strength, $\tilde{\varepsilon}_w$. The figure presents data for two different interaction ranges, σ_w, as indicated in the key. (b) Membrane tension, $\tilde{\gamma} = \gamma R_0^2/\kappa$, as a function of adhesion strength, $\tilde{\varepsilon}_w$.

For λ_E, we first determine the value, C_{1max}. Then, λ_E is estimated from eqn (31) by a one-parameter fit in the vicinity of $r \gtrsim r_E$, as illustrated by the dashed lines in Fig. 4d.

The comparison of the two data sets with different ranges, σ_w, of membrane–substrate interactions reveals that this local characteristic is largely independent of σ_w, similar to the behavior of the transversality condition.

The three different estimates, however, differ for small $\tilde{\varepsilon}_w$ and only appear to converge to a common value for large adhesion strength. Given the involved approximation, $r_E \ll \lambda_\gamma$, these deviations are expected. For small adhesion strength, $\tilde{\varepsilon}_w$, the vesicle is nearly spherical and the geometry-dependent tension is very small. Upon increasing $\tilde{\varepsilon}_w$, we observe a rather pronounced decrease of λ_γ. λ_E obtained from the decay of the curvature at the edge of the adhesion zone also decreases with the adhesion strength, $\tilde{\varepsilon}_w$, but the dependence is significantly weaker. The estimate, λ_1, that is extracted from the overall shape of the vesicle, assuming a cap shape, even displays the opposite $\tilde{\varepsilon}_w$-dependence at small adhesion strength. This finding highlights the challenge of accurately estimating the membrane–vesicle interactions *via* analytical but approximate descriptions of the vesicle shape.

The experimentally determined height profiles were fitted with eqn (30) up to $z \approx 300$ nm. As reported previously,[20,21] α was determined by the intersection of the linear fit (black line) with the abscissa with λ_E determined from the fit (Fig. 8c).

Independent of the specific functional form, eqn (30), of the fit of the vesicle profile at the adhesion edge, we utilize the fit to compute the contact curvature $C_{1max} = \frac{\alpha}{\lambda_E}$. In Fig. 8d, the contact curvature C_{1max} was plotted *versus* the vesicle radius at the plane of the equator, R_{eq}. As expected, C_{1max}, is independent of the vesicle size.

Using the previously reported bending rigidity of DOPC vesicles, $\kappa = 24k_BT$,[46] and the transversality condition, eqn (22), our experimental data (Fig. 8d) yielded the average adhesion free energy, $\Delta\gamma_w \approx 41k_BT/\mu m^2$, which is comparable with the free energy of integrin-mediated vesicle adhesion.[20,21] Depending on the vesicle size, R_0, these values give rise to a dimensionless

adhesion strength of $\tilde{\varepsilon}_w = \Delta\gamma_w R_0^2/\kappa \approx 1.71(R_0/\mu m)^2 \approx 7$ or 84 for $R_0 = 2$ μm and 7 μm, respectively. Thus, the experimental data are in the strong adhesion regime, $\tilde{\varepsilon}_w \gg 2$.

Analogously, the adhesion free energy at $[CdCl_2] = 0.25$ mM, $\Delta\gamma_w \approx 24 k_B T/\mu m^2$ was calculated.

3.5 Modulation of interfacial potential $V(z)$ calculated from experimental data

To quantitatively determine the curvature of the effective membrane–substrate potential, $V(z)$, between vesicles and substrates coated with PAA-Cys5 brushes, we monitored the height fluctuation of adhesion zones by recording RICM movies over time. As averaging the signal intensity over a large membrane patch or the camera's shot noise could smear the local membrane height fluctuation due to the macroscopic membrane undulation and the shot noise,[63] we selected 3 small regions (3×3 pixels corresponding to 0.096 μm^2) near the center of the adhesion zone and monitored the mean intensity fluctuation inside each region (Fig. 10a). Using eqn (3) we computed the laterally averaged height fluctuations, $\delta z = \bar{z} - \langle z \rangle$ where $\bar{z}$ stands for the lateral average of the membrane height in a small 3×3 pixel region and $\langle z \rangle = 0$ denotes the height average over the entire membrane patch of macroscopic dimension, L.

Panel (b and c) of Fig. 10 show the height fluctuations, $\delta z(t)$, monitored at 30 ms per frame for 12 s and the distribution of fluctuation amplitudes, $P(\delta z)$, measured at $[CdCl_2] = 0.25$ mM (grey) and 1.0 mM (black), respectively. As shown in Fig. 10c, $P(\delta z)$ determined by experiments are well approximated by a Gaussian distribution.

In order to extract the curvature, $V'' \equiv d^2V/dz^2|_{z=0}$, of the membrane–substrate interaction from the measured variance, $\langle \delta z^2 \rangle$, we consider an almost planar membrane patch, $|\nabla z| \ll 1$, in contact with the substrate and use the Monge representation

$$\mathcal{H}_0[z] = \int dx\, dy \left\{ V(z) + \gamma + \frac{\gamma}{2}(\nabla z)^2 + \frac{\kappa}{2}(\Delta z)^2 \right\} \quad (32)$$

Quadratically expanding the membrane–substrate interaction around its minimum at $z = 0$ yields

$$V(z) = -\Delta\gamma_w + \frac{1}{2}V'' z^2 + \mathcal{O}(z^3) \quad (33)$$

and assuming that the membrane tension is negligible, $\gamma \approx 0$, we obtain

$$\frac{\mathcal{H}_0[\tilde{z}]}{L^2} = -\Delta\gamma_w + \frac{1}{2}V''\tilde{z}_0^2 + \frac{1}{2}\sum_{q \neq 0}(V'' + \kappa q^4)|\tilde{z}_q|^2 \quad (34)$$

where $\tilde{z}_q$ denotes the two-dimensional Fourier transform of $z(x,y)$ and L the length of a membrane patch. In equilibrium, the Fourier modes are Gaussian distributed with zero mean and variance

$$\langle \tilde{z}_q \tilde{z}_{q'} \rangle = \frac{k_B T}{L^2(V'' + \kappa q^4)}\delta_{q,-q'} \quad (35)$$

On short length scales, the bending rigidity, κ, dominates the fluctuation spectrum, whereas the curvature of the membrane–substrate potential dictates the fluctuation of the physically coupled membrane on large scales. The crossover is set by the parallel correlation length, $\xi_\parallel \equiv \sqrt[4]{\kappa/V''}$.

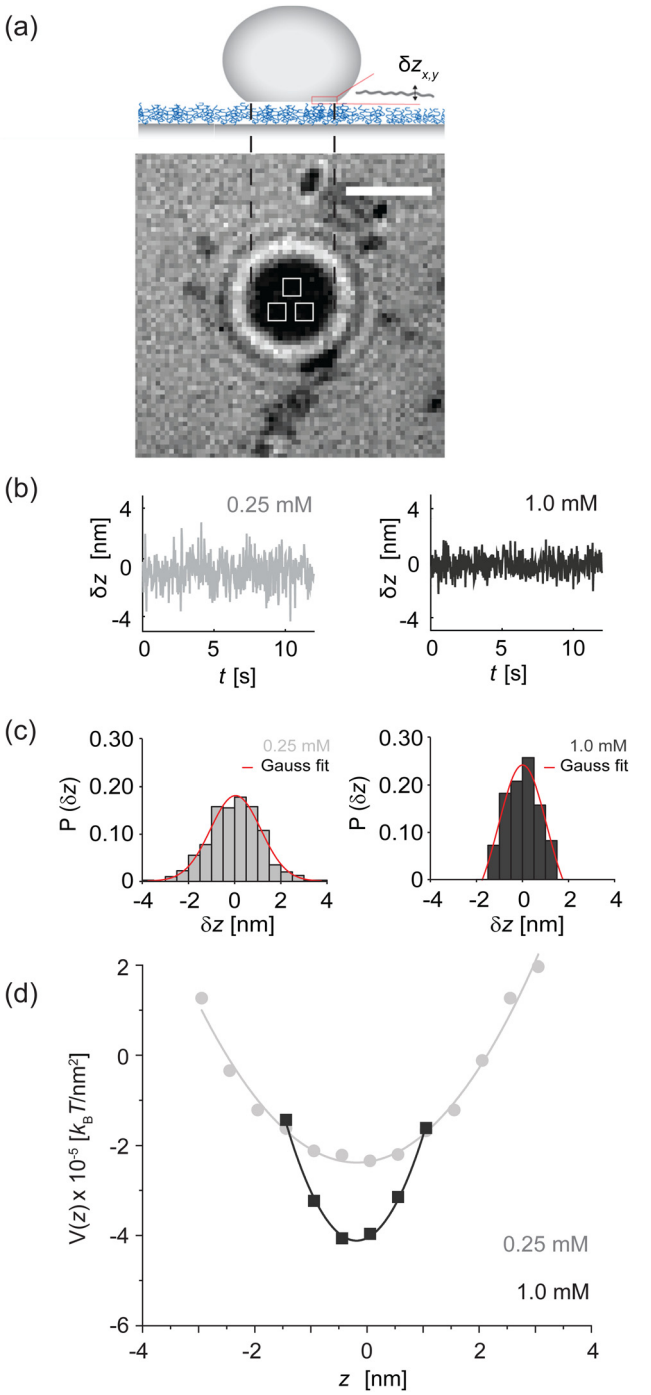

Fig. 10 Modulation of membrane fluctuation by $[CdCl_2]$. (a) The intensity fluctuations collected from three independent locations in the adhesion zone (3×3 pixels each, indicated by white boxes) were converted to the height fluctuation following eqn (3). Scale bar: 2 μm. (b) Laterally averaged membrane–substrate distance, δz, plotted *versus* time at $[CdCl_2] = 0.25$ mM (grey) and 1 mM (black). (c) Probability of fluctuation amplitude $P(\delta z)$ calculated from the data presented in panel b. (d) Effective membrane–substrate potential, $V(z)$ calculated *versus* z. The potential curvature $V''(z = 0)$ or the "spring constant" represents the sharpness of membrane confinement, while the potential minima correspond to the adhesion free energy $\Delta\gamma_w$ determined by microinterferometry.[8]

The resolution of microscopy is determined by the pixel size which is 103 nm for the microscope used in this study. Thus the membrane fluctuation is laterally averaged over a scale $\Delta_{3p} \gg \xi_{\parallel}$

$$\delta z \equiv \frac{1}{{\Delta_{3p}}^2}\int_{{\Delta_{3p}}^2} \mathrm{d}x\mathrm{d}y\; z(x,y) = \sum_{\mathbf{q}\neq 0} \tilde{z}_{\mathbf{q}} \frac{2\sin\frac{q_x\Delta_{3p}}{2}}{q_x\Delta_{3p}} \frac{2\sin\frac{q_y\Delta_{3p}}{2}}{q_y\Delta_{3p}} \quad (36)$$

Using eqn (35) and (36), we calculate $\langle \delta z^2 \rangle$

$$\langle \delta z^2 \rangle = \frac{k_{\mathrm{B}}T}{V''(2\Delta_{3p})^2} \quad (37)$$

This analysis allows us to estimate the curvature of the membrane–substrate interaction, V'', near the average height of an adhered membrane patch. We extracted the variance of the height fluctuations from Fig. 10b and c, and calculated, $V''_{0.25\mathrm{mM}} = k_{\mathrm{B}}T/[\langle \delta z^2 \rangle (2\Delta_{3p})^2] = 2.5 \pm 1.8 \times 10^{-6} k_{\mathrm{B}}T/\mathrm{nm}^4$ and $V''_{1.0\mathrm{mM}} = 3.9 \pm 0.9 \times 10^{-6} k_{\mathrm{B}}T/\mathrm{nm}^4$ (n = 15), for the two Cd^{2+} ion concentrations respectively. The clear increase in V'' caused by a subtle increase in $[CdCl_2]$ implied that the membrane patch in the adhesion zone is more sharply confined near the brush-coated substrate. As shown in Fig. 10c, the probability of local height fluctuation, $P(\delta z)$, is well approximated by a Gaussian and thus the shape of the potential in Fig. 10d resembles the orange curve, V_{c}, depicted in Fig. 3, at least in the vicinity of the minimum at z = 0.

It should be noted that the microinterferometric analysis of membrane height fluctuation enables to characterize the potential curvature V'' corresponding to the ''spring constant'' of a harmonic oscillator but not the absolute potential energy minimum $\Delta\gamma_{\mathrm{w}}$, *i.e.*, the adhesion energy per unit area. Therefore, we took the experimentally determined mean squared amplitude of fluctuation $\langle \delta z^2 \rangle$ and adhesion free energy $\Delta\gamma_{\mathrm{w}}$ and calculated the absolute interfacial potential $V(z)$ using eqn (33). In Fig. 10d the absolute interfacial potentials for the different Cd^{2+} ion concentrations are shown, which results in potential minima of $\Delta\gamma_{\mathrm{w,0.25mM}} \approx 24 k_{\mathrm{B}}T/\mu\mathrm{m}^2$ and $\Delta\gamma_{\mathrm{w,1.0mM}} \approx 41 k_{\mathrm{B}}T/\mu\mathrm{m}^2$.

Using vesicles adhering to micropatterned steps, Schmidt *et al.* showed that the membrane–substrate potential of vesicles becomes nonharmonic,[63] which takes a similar shape as the blue curve presented in Fig. 3. The main difference between the two experimental systems is that the amplitude of height fluctuation on our PAA-Cys5 brushes is several nm, indicating that the membrane is confined in the close vicinity of the potential minimum. On the other hand, the membrane on micropatterned steps fluctuates by tens of nm where the long-range interactions can be detected due to a large membrane–substrate distance ($\sim$100 nm).

4 Conclusions

We synthesized a cysteine-modified polyacrylic acid polymer, PAA-Cys5, that changes the conformation in the presence of Cd^{2+} ions in a concentration-dependent fashion, and grafted the brushes on supported membranes at the controlled grafting distance $\langle d \rangle$ = 6 nm. Specular X-ray reflectivity data indicated the compaction of PAA-Cys5 layer at $[CdCl_2]$ = 1 mM (Fig. 6), which modulates the wetting by the phospholipid vesicles by varying Cd^{2+} ion concentrations. As the onset of stable contact zones is strongly linked to an increase in potential strength, we can reference this to the change in brush conformation. Thus, by carefully observing the vesicle–brush contact zone by micro-interferometry, we observed the onset of wetting at, $[CdCl_2]$ = 0.25 mM (Fig. 7). The analysis of the height fluctuation of membranes and the shape of vesicles near the substrate enabled us to determine the curvature of the membrane–substrate interaction, $V''(z)$ (Fig. 10), contact curvature $C_{1\mathrm{max}}$, and the adhesion free energy $\Delta\gamma_{\mathrm{w}}$ (Fig. 8).

We have studied the shape and thermodynamics of vesicles on stimulus responsive substrates. Whereas most previous studies focus on the idealized situation of zero-ranged contact interaction in the absence of buoyancy (see ref. 39 and 40 for exceptions), we pay particular attention to the potential range as this is relevant to experiments. However, the long-range potential has only a minor influence on the maximal curvature at the edge of the adhesion zone (see Fig. 5), slightly adapting the coefficient of the transversality condition that is commonly employed to relate the contact curvature to the adhesion strength, given a scale separation between potential range and vesicle size. We want to emphasize, that the combination of simulation and experiment enables us to determine the absolute interfacial potential $V(z)$ with $\Delta\gamma_{\mathrm{w}}$ as the potential minimum.

Author contributions

MN synthesized the polymer. FW performed the experiment and analyzed the experimental data. LW supported the data analysis and performed the simulations. MM and MT designed the research, acquired funding, and supervised the project. FW, LW, MM, and MT discussed the data, and all the authors contributed to writing the manuscript.

Conflicts of interest

There are no conflicts to declare.

Acknowledgements

The authors thank the Deutsche Forschungsgemeinschaft (DFG) within the priority program SPP2171 under grant numbers Mu1674/17-1 (to MM) and Ta253/14-1 (to MT), and the JSPS KAKANHI under the grant number JP19H05719 (to MT and MN) for financial supports. FW thanks Nikon Imaging Center Heidelberg for the support to confocal microscopy imaging. LW and MM gratefully acknowledge the Gauss Centre for Supercomputing e.V. (**www.gauss-centre.eu**) for funding this research project by providing computing time through the John von Neumann Institute for Computing (NIC) on GCS Supercomputer JUWELS at the Jülich Supercomputing Centre (JSC). MT thanks Nakatani Foundation for support.

Notes and references

1 R. L. Juliano, *Annu. Rev. Pharmacol. Toxicol.*, 2002, **42**, 283–323.
2 E. Sackmann and M. Tanaka, *Biophys. Rev.*, 2021, **13**, 123–138.
3 C.-P. Heisenberg and Y. Bellache, *Cell*, 2013, **153**, 948–962.
4 U. Cavallaro and G. Christofori, *Nat. Rev. Cancer*, 2004, **4**, 118–132.
5 A. Gierer, S. Berking, H. Bode, C. N. David, K. Flick, G. Hansmann, H. Schaller and E. Trenkner, *Nat. New Biol.*, 1972, **239**, 98–101.
6 U. Technau and T. W. Holstein, *Dev. Biol.*, 1992, **151**, 117–127.
7 S. K. Bromley, W. R. Burack, K. G. Johnson, K. Somersalo, T. N. Sims, C. Sumen, M. M. Davis, A. S. Shaw, P. M. Allen and M. L. Dustin, *Annu. Rev. Immunol.*, 2001, **19**, 375–396.
8 G. S. G. Balta, C. Monzel, S. Kleber, J. Beaudouin, E. Balta, T. Kaindl, S. Chen, L. Gao, M. Thiemann, C. R. Wirtz, Y. Samstag, M. Tanaka and A. Martin-Villalba, *Cell Rep.*, 2019, **29**, 2295–2306.e6.
9 S. Komura and D. Andelman, *Eur. Phys. J. E*, 2000, **3**, 259–271.
10 B. Froöhlich, A. K. Dasanna, C. Lansche, J. Czajor, C. P. Sanchez, M. Cyrklaff, A. Yamamoto, A. Craig, U. S. Schwarz, M. Lanzer and M. Tanaka, *Biophys. J.*, 2021, **120**, 3315–3328.
11 G. I. Bell, M. Dembo and P. Bongrand, *Biophys. J.*, 1984, **45**, 1051.
12 U. Seifert and R. Lipowsky, *Phys. Rev. A: At., Mol., Opt. Phys.*, 1990, **42**, 4768–4771.
13 R. Lipowsky and U. Seifert, *Langmuir*, 1991, **7**, 1867–1873.
14 R. Bruinsma and E. Sackmann, *C. R. Acad. Sci., Ser. IV: Phys., Astrophys.*, 2001, **2**, 803–815.
15 W. Helfrich, *Z. Naturforsch.*, 1973, **28c**, 693–703.
16 G. Gompper and D. M. Kroll, *J. Phys. I*, 1996, **6**, 1305–1320.
17 G. Gueguen, N. Destainville and M. Manghi, *Soft Matter*, 2017, **13**, 6100–6117.
18 Y. Thomas, *Philos. Trans. R. Soc. London*, 1805, **95**, 65–87.
19 M. Tanaka and E. Sackmann, *Nature*, 2005, **437**, 656–663.
20 S. Goennenwein, M. Tanaka, B. Hu, L. Moroder and E. Sackmann, *Biophys. J.*, 2003, **85**, 646–655.
21 O. Purrucker, A. Förtig, R. Jordan, E. Sackmann and M. Tanaka, *Phys. Rev. Lett.*, 2007, **98**, 078102.
22 F. F. Rossetti, E. Schneck, G. Fragneto, O. V. Konovalov and M. Tanaka, *Langmuir*, 2015, **31**, 4473–4480.
23 S. Minko, M. Müller, M. Motornov, M. Nitschke, K. Grundke and M. Stamm, *J. Am. Chem. Soc.*, 2003, **125**, 3896–3900.
24 C. D. L. H. Alarcón, S. Pennadam and C. Alexander, *Chem. Soc. Rev.*, 2005, **34**, 276–285.
25 H. Merlitz, G.-L. He, J.-U. Sommer and C.-X. Wu, *Macromolecules*, 2009, **42**, 445–451.
26 O. Hoy, B. Zdyrko, R. Lupitskyy, R. Sheparovych, D. Aulich, J. Wang, E. Bittrich, K.-J. Eichhorn, P. Uhlmann, K. Hinrichs, M. Müller, M. Stamm, S. Minko and I. Luzinov, *Adv. Funct. Mater.*, 2010, **20**, 2240–2247.
27 M. A. C. Stuart, W. T. S. Huck, J. Genzer, M. Müller, C. Ober, M. Stamm, G. B. Sukhorukov, I. Szleifer, V. V. Tsukruk, M. Urban, F. Winnik, S. Zauscher, I. Luzinov and S. Minko, *Nat. Mater.*, 2010, **9**, 101–113.
28 A. D. Price, S.-M. Hur, G. H. Fredrickson, A. L. Frischknecht and D. L. Huber, *Macromolecules*, 2012, **45**, 510–524.
29 F. Léonforte, U. Welling and M. Müller, *J. Chem. Phys.*, 2016, **145**, 224902.
30 T. E. Brown and K. S. Anseth, *Chem. Soc. Rev.*, 2017, **46**, 6532–6552.
31 M. Tanaka, M. Nakahata, P. Linke and S. Kaufmann, *Polym. J.*, 2020, **52**, 861–870.
32 F. Rehfeldt, R. Steitz, S. P. Armes, R. von Klitzing, A. P. Gast and M. Tanaka, *J. Phys. Chem. B*, 2006, **110**, 9171–9176.
33 F. Jalilehvand, Z. Amini, K. Parmar and E. Y. Kang, *Dalton Trans.*, 2011, **40**, 12771–12778.
34 T. Kaindl, H. Rieger, L.-M. Kaschel, U. Engel, A. Schmaus, J. Sleeman and M. Tanaka, *PLoS One*, 2012, **7**, e42991.
35 H. Rieger, H. Y. Yoshikawa, K. Quadt, M. A. Nielsen, C. P. Sanchez, A. Salanti, M. Tanaka and M. Lanzer, *Blood*, 2015, **125**, 383–391.
36 C. Helm, W. Knoll and J. Israelachvili, *Proc. Natl. Acad. Sci. U. S. A.*, 1991, **88**, 8169–8173.
37 J. Nardi, T. Feder, R. Bruinsma and E. Sackmann, *Europhys. Lett.*, 1997, **37**, 371–376.
38 J. Nardi, R. Bruinsma and E. Sackmann, *Phys. Rev. Lett.*, 1999, **82**, 5168–5171.
39 U. Seifert, *Phys. Rev. A: At., Mol., Opt. Phys.*, 1991, **43**, 6803–6814.
40 M. Kraus, U. Seifert and R. Lipowsky, *Europhys. Lett.*, 1995, **32**, 431–436.
41 C. Tordeux, J. B. Fournier and P. Galatola, *Phys. Rev. E: Stat., Nonlinear, Soft Matter Phys.*, 2002, **65**, 041912.
42 W. T. Góźdź, *Langmuir*, 2004, **20**, 7385–7391.
43 J. Raval and W. T. Góźdź, *ACS Omega*, 2020, **5**, 16099–16105.
44 W. Kern and D. Puotinen, *RCA Rev.*, 1983, **31**, 187–206.
45 H. Hillebrandt and M. Tanaka, *J. Phys. Chem. B*, 2001, **105**, 4270–4276.
46 T. Matsuzaki, H. Ito, V. Chevyreva, A. Makky, S. Kaufmann, K. Okano, N. Kobayashi, M. Suganuma, S. Nakabayashi and H. Y. Yoshikawa, *et al.*, *Phys. Chem. Chem. Phys.*, 2017, **19**, 19937–19947.
47 L. G. Parratt, *Phys. Rev.*, 1954, **95**, 359–369.
48 A. Nelson, *J. Appl. Crystallogr.*, 2006, **39**, 273–276.
49 A. Albersdörfer, T. Feder and E. Sackmann, *Biophys. J.*, 1997, **73**, 245–257.
50 L. Limozin and K. Sengupta, *ChemPhysChem*, 2009, **10**, 2752–2768.
51 E. Evans, *Colloids Surf.*, 1990, **43**, 327–347.
52 R. Lipowsky and E. Sackmann, *Structure and dynamics of Membranes*, Elsevier Science, 1995.
53 N. Frenkel, A. Makky, I. R. Sudji, M. Wink and M. Tanaka, *J. Phys. Chem. B*, 2014, **118**, 14632–14639.
54 A. Makky and M. Tanaka, *J. Phys. Chem. B*, 2015, **119**, 5857–5863.
55 A. Yamamoto, K. Hayashi, A. Sumiya, F. Weissenfeld, S. Hinatsu, W. Abuillan, M. Nakahata and M. Tanaka, *Front. Soft. Matter.*, 2022, **2**, 959542.
56 J. Nardi, R. Bruinsma and E. Sackmann, *Phys. Rev. E: Stat. Phys., Plasmas, Fluids, Relat. Interdiscip. Top.*, 1998, **58**, 6340.

57 L. J. Lis, V. A. Parsegian and R. P. Rand, *Biochemistry*, 1981, **20**, 1761–1770.
58 D. H. Hamer, *Ann. Rev. Biochem.*, 1986, **55**, 913–951.
59 C. S. Cobbett, *Curr. Opin. Plant Biol.*, 2000, **3**, 211–216.
60 M.-T. Nistor, D. Pamfil, C. Schick and C. Vasile, *Thermochim. Acta*, 2014, **589**, 114–122.
61 Z. Guttenberg, A. R. Bausch, B. Hu, R. Bruinsma, L. Moroder and E. Sackmann, *Langmuir*, 2000, **16**, 8984–8993.
62 R. Bruinsma, *Physics of Biomaterials, Physical aspects of adhesion of leukocytes*, Kluwer, Dordrecht, 1995, pp. 61–102.
63 D. Schmidt, C. Monzel, T. Bihr, R. Merkel, U. Seifert, K. Sengupta and A.-S. Smith, *Phys. Rev. X*, 2014, **4**, 021023.

